Hierarchical NiCo$_2$O$_4$@NiCo$_2$O$_4$ Core/Shell Nanoflake Arrays as High-Performance Supercapacitor Materials

Xiayuan Liu, Shaojun Shi, Qinqin Xiong, Lu Li, Yijun Zhang, Hong Tang, Changdong Gu, Xiuli Wang, and Jiangping Tu*

State Key Laboratory of Silicon Materials, Key Laboratory of Advanced Materials and Applications for Batteries of Zhejiang Province, and Department of Materials Science and Engineering, Zhejiang University, Hangzhou 310027, China

S *Supporting Information*

ABSTRACT: Hierarchical NiCo$_2$O$_4$@NiCo$_2$O$_4$ core/shell nanoflake arrays on nickel foam for high-performance supercapacitors are fabricated by a two-step solution-based method which involves in hydrothermal process and chemical bath deposition. Compared with the bare NiCo$_2$O$_4$ nanoflake arrays, the core/shell electrode displays better pseudocapacitive behaviors in 2 M KOH, which exhibits high areal specific capacitances of 1.55 F cm^{-2} at 2 mA cm^{-2} and 1.16 F cm^{-2} at 40 mA cm^{-2} before activation as well as excellent cycling stability. The specific capacitance can achieve a maximum of 2.20 F cm^{-2} at a current density of 5 mA cm^{-2}, which can still retain 2.17 F cm^{-2} (98.6% retention) after 4000 cycles. The enhanced pseudocapacitive performances are mainly attributed to its unique core/shell structure, which provides fast ion and electron transfer, a large number of active sites, and good strain accommodation.

KEYWORDS: *spinel nickel cobaltate, core/shell structure, porous film, supercapacitor, hydrothermal method, chemical bath deposition*
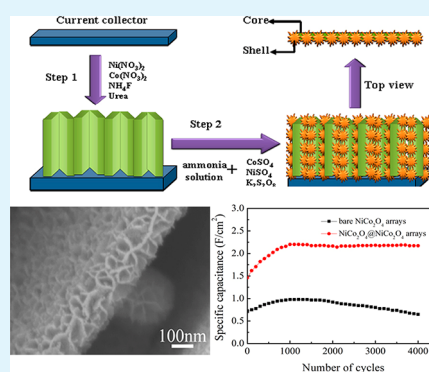
1. INTRODUCTION

The growing interests in electric vehicles allied with the ubiquity of increasingly capable mobile devices create a seemingly insatiable demand for electrochemical energy storage with higher power and energy densities. Electrochemical capacitors, also called supercapacitors, offering transient but extremely high powers, are probably the most important next-generation energy storage device.[1−8]

To date, various materials, including carbonaceous materials, transition metal oxides,[9−12] conducting polymers,[13] and hybrid composites,[14−17] have been widely studied as electrodes for supercapacitors. Among them, hydrous RuO$_2$ exhibits the highest performance to date, but the scarcity in nature and high cost limit its commercial application. Therefore, great efforts have been devoted to searching for inexpensive alternative transition metal oxides with good capacitive characteristics,[7,9,18−21] specially those who possess multiple oxidation states/structures that enable rich redox reactions, such as Co$_3$O$_4$,[9,10,22,23] NiO,[24−26] MnO$_2$,[11,27,28] hydroxide-based composites,[11] and Co$_3$O$_4$/NiO core/shell nanowire arrays.[29] Recently, ternary NiCo$_2$O$_4$ has drawn intensive research attention because it is low-cost, environmentally benign, and naturally abundant and has a high theoretical capacitance. Besides, it is expected to offer richer redox reactions, including contributions from both nickel and cobalt ions, than the two corresponding single-component oxides and is a potential cost-effective alternative for RuO$_2$.[30−43]

However, transition metal oxides including NiCo$_2$O$_4$ usually showed limited kinetics during the redox reaction as a result of their low electrical conductivity and low surface area.[2,3,31,44−48] Besides, the short diffusion distance of electrolyte into supercapacitor electrodes made the underneath parts hardly participate in the electrochemical charge storage process, leading to a less satisfactory areal specific capacitance (ASC). Therefore, to meet the requirements of high ASC, specific capacitance, structural stability and boost the electrochemical utilization of the active materials, one promising route is to have scrupulous design of nanoarchitectures and smart hybridization of bespoke pseudocapacitive oxides. Recently, tremendous efforts have been devoted to the synthesis of advanced core/shell nanowire heterostructures with the combination of two types of materials which show improved electrochemical performances.[1,13−17,45,49−53] However, to the best of our knowledge, there is little work on rational design of a homogeneous core/shell nanoflake arrays for supercapacitors, though the capacitive property of the core/shell nanowire arrays with the combination of two types of materials has been extensively investigated. As we know, with the same mass weight, the surface area of the nanoflake is much higher than that of the nanowire. Besides, the interconnected flake network makes the electrode much stable toward cycling. On the basis of the above considerations, one would expect a novel NiCo$_2$O$_4$@NiCo$_2$O$_4$ core/shell nanoflake arrays to be a promising candidate for the construction of high-performance

supercapacitors. In this electrode design, not only are both the "core" and "shell" materials be effectively utilized but additionally a strong synergistic effect can be realized.

In this present work, a novel $NiCo_2O_4$@$NiCo_2O_4$ core/shell nanoflake array is synthesized on Ni foam via a two-step solution route coupled with a post calcination treatment. The ultrathin $NiCo_2O_4$ nanoflakes synthesized by hydrothermal method are the "core", whereas the $NiCo_2O_4$ nanoflakes prepared by chemical bath deposition (CBD) are the "shell". Impressively, compared with the bare $NiCo_2O_4$ arrays electrode, the core/shell one exhibits noticeable electrochemical performance with higher capacitance as well as better cycling stability. Because of the unique properties, such as fast ion and electron transfer, large numbers of active sites and good strain accommodation, these core/shell nanoflake arrays have potential applications in energy storage.

2. EXPERIMENTAL SECTION

2.1. Preparation of $NiCo_2O_4$@$NiCo_2O_4$ Core/Shell Nanoflake Arrays. First, $NiCo_2O_4$ nanoflake arrays were synthesized on nickel foam by a facile hydrothermal method. The experimental details were as follows. One mmol of $Ni(NO_3)_2$, 2 mmol of $Co(NO_3)_2$, 6 mmol of NH_4F, and 15 mmol of urea were dissolved in 70 mL of deionized water under magnetical stirring for 30 min in air. Then the resulting solution was transferred into a 100 mL Teflon-lined stainless steel autoclave and the nickel foam substrate with 3.5×5.0 cm in size was immersed into it. After that, the autoclave was heated to 120 °C inside a conventional oven for 3 h, and then cooled to room temperature. Subsequently, the pink precursor was removed from the solution and washed with distilled water repeatedly. Because the precursor is cobalt−nickel hydroxide, it converts into cobalt−nickel oxide after annealing at 350 °C for 2 h in flowing argon.

Then, the self-supported $NiCo_2O_4$ nanoflake arrays were used as the scaffold for further $NiCo_2O_4$ growth in a simple chemical bath. The $NiCo_2O_4$ nanoflake arrays grown on nickel foam were placed vertically in a 250 mL Pyrex beaker. Solution for chemical bath deposition (CBD) was prepared by adding 20 mL of aqueous ammonia (25−28%) to the mixture of 50 mL of 1 M nickel sulfate, 50 mL of 2 M cobalt sulfate, and 80 mL of 0.25 M potassium peroxydi sulfate. The samples were placed in the solution for 8 min to deposit the shell precursor. Finally, the precursor was annealed at 350 °C in argon for 2 h. The total loading mass of the $NiCo_2O_4$@$NiCo_2O_4$ core/shell nanoflake arrays is 1.97 mg cm^{-2}, with a loading mass of 1.34 and 0.63 mg for the core and the shell $NiCo_2O_4$, respectively.

2.2. Structural Characterization. The structures and morphologies of the products were characterized by X-ray diffraction (XRD, RIGAKU D/Max-2550 with Cu Kα radiation), field emission scanning electron microscopy (FESEM, FEI SIRION) and transmission electron microscopy (TEM, JEOL JEM200CX, JEM-2010F) with an X-ray energy-dispersive spectroscope (EDS, BRUKER AXS).

2.3. Electrochemical Measurements. A three-electrode cell was used for electrochemical measurements with the as-prepared arrays as the working electrode, and a nickel mesh and Hg/HgO as the counter and reference electrodes, respectively. 2.0 M KOH aqueous solution was used as the electrolyte. Cyclic voltammetry (CV) tests were performed on a CHI660d electrochemical workstation (Chenhua, Shanghai) at a scanning rate of 10 mV s^{-1} between 0.1 and 0.65 V at room temperature. Electrochemical impedance spectroscopy (EIS) measurements were carried out on this apparatus with a superimposed 5 mV sinusoidal voltage in the frequency range of 100 kHz to 0.01 Hz. The galvanostatic charge−discharge tests were conducted on a LAND battery program-control test system. The specific capacitance is calculated according to the following equation

$$C = \frac{I\Delta t}{M\Delta V} \qquad (1)$$

where C (F g^{-1}) is the specific capacitance, I (mA) represents the discharge current, and M (mg), ΔV (V), and Δt (s) designates the mass of active materials, potential drop during discharge, and total discharge time, respectively.

3. RESULTS AND DISCUSSION

3.1. Synthesis and Characterization. Our approach for fabricating $NiCo_2O_4$@$NiCo_2O_4$ core/shell nanoflake arrays as pseudocapacitive electrode involves two key steps, as shown in Scheme 1. First, aligned $NiCo_2O_4$ core nanoflake arrays are

Scheme 1. Schematic Illustration of the Two-Step Synthesis of $NiCo_2O_4$@$NiCo_2O_4$ Core/Shell Nanoflake Arrays Directly on Ni Foam Substrate
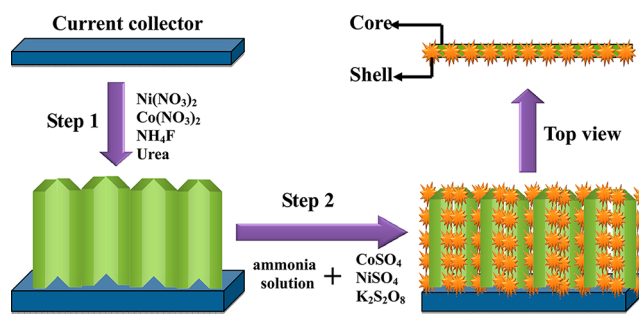
deposited on Ni foam substrate. Subsequently, a thin layer of $NiCo_2O_4$ is coated onto the surface of the as-prepared $NiCo_2O_4$ core nanoflakes, forming the hierarchical $NiCo_2O_4$@$NiCo_2O_4$ core/shell nanoflake arrays.

Figure 1 shows the XRD patterns of the bare $NiCo_2O_4$ and $NiCo_2O_4$@$NiCo_2O_4$ core/shell nanoflake arrays on nickel
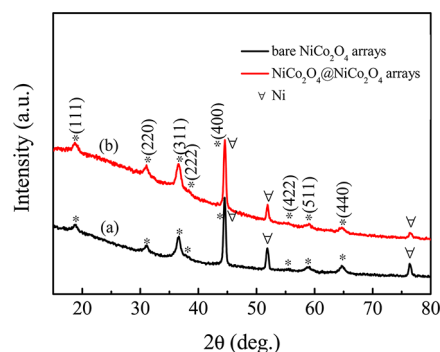

Figure 1. XRD patterns of (a) the bare $NiCo_2O_4$ array and (b) the $NiCo_2O_4$@$NiCo_2O_4$ core/shell nanoflake array.

foam. For the bare nanoflake arrays, all the reflection peaks beside the nickel foam substrate can be well indexed to spinel $NiCo_2O_4$ phase (JCPDS 73−1702) (Figure 1a). For the core/shell nanoflake arrays (Figure 1b), the pattern shows little difference with the bare one. There are no extra peaks in the pattern, indicating that the shell material is also $NiCo_2O_4$. However, the diffraction peaks of the $NiCo_2O_4$@$NiCo_2O_4$ core/shell nanoflake arrays is broader than those of the bare one, indicating that the size of shell $NiCo_2O_4$ crystals are smaller, or lower crystallinity of them.

Morphologies of the bare $NiCo_2O_4$ before CBD process and the core−shell nanoflakes were examined using SEM. The bare $NiCo_2O_4$ nanoflakes cover uniformly on the substrate surface after hydrothermal process, as can be seen from Figure 2a. The formation of the nanoflake film is based on heterogeneous nucleation and growth due to the lower interfacial nucleation
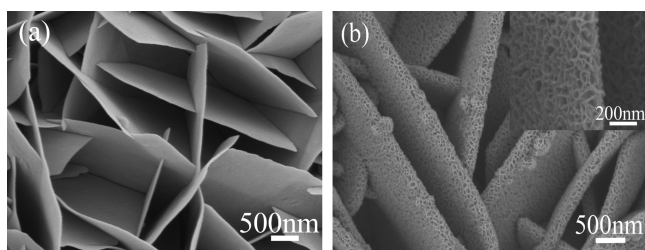
Figure 2. SEM images of (a) the bare $NiCo_2O_4$ nanoflake array and (b) the $NiCo_2O_4@NiCo_2O_4$ core/shell nanoflake array grown on Ni foam substrate.

energy on the substrate. Besides, the nanoflakes are ultrathin, which can do benefit to the fully utilization of the active materials. Figure 2b illustrates the core–shell nanoflake film after CBD process. Apparently thickness of the whole nanoflakes increases and the surface is covered by numerous leaf-like ultrathin nanoflakes, forming highly porous core–shell architecture. The nanoflake shells are interconnected but still do not fully cover the entire core. The pores or voids between nanoplatelets of both the core and shell will act as effective transportation channels for the electrolyte during charge–discharge process. Thus, nearly all the core/shell nanoflakes are highly accessible to electrolyte to obtain a high specific capacitance. Besides, as both the "core" and the "shell" are ultrathin, the electrolyte can diffuse into the underneath part of the electrode materials, so all the active materials can participate in the electrochemical charge storage process, leading to a higher area specific capacitance.

The growing process of the $NiCo_2O_4$ shell is studied by inspecting the morphologies at different growth stages (Figure 3). At the early stage (deposition for 1.5 min, Figure 3a), one
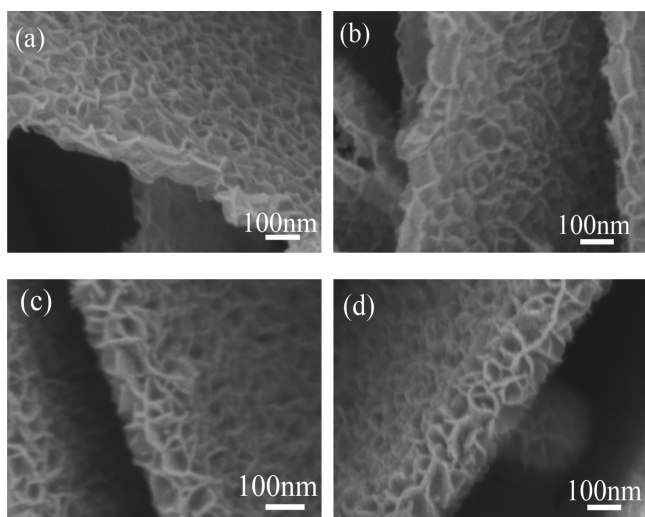

Figure 3. SEM images of the $NiCo_2O_4@NiCo_2O_4$ core/shell nanoflake arrays obtained by chemical bath deposition for various times: t = (a) 1.5, (b) 3, (c) 6, and (d) 8 min.

can see that the nanoparticles start to attach to the surface of the core nanoflakes. As the deposition proceeds, the $NiCo_2O_4$ shell begins to grow and the mass of the shell increases accordingly. The thickness of the $NiCo_2O_4$ shell can be easily controlled by changing the CBD reaction time. This provides us with the ability to tune the structure of the core/shell nanoflake arrays.

The as-prepared arrays were scratched down from the Ni foam, and the structural characteristics of the bare nanoflakes and the core/shell nanoflakes were analyzed. As shown in images a and b in Figure 4, the $NiCo_2O_4$ core nanoflakes are
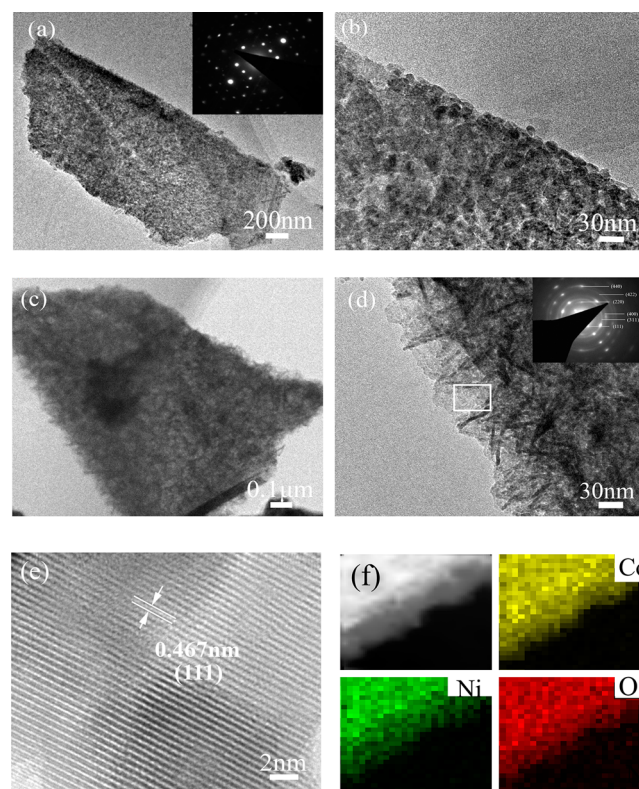

Figure 4. TEM characterization of (a, b) the bare $NiCo_2O_4$ nanoflake and (c) the $NiCo_2O_4@NiCo_2O_4$ core/shell nanoflake, (d) shell of the core/shell nanoflake (inset: SAED pattern of the shell), (e) HRTEM images of the shell, (f) EDS of element Co, Ni, and O.

highly porous, composed of nanocrystallites of 10−20 nm. They are well crystallized in whole, as revealed by the selected area electronic diffraction (SAED) pattern (inset of Figure 4a). For the $NiCo_2O_4@NiCo_2O_4$ core/shell nanoflakes, the typical TEM image in Figure 4c shows clearly that the porous $NiCo_2O_4$ is enclosed by a thin and continuous layer. A close examination of the exposed profile reveals that the thickness of the outer shell is about 60 nm (Figure 4d). The corresponding SAED pattern of the shell shows well-defined rings, indicating the polycrystalline characteristic of $NiCo_2O_4$ (inset of Figure 4d). High-resolution TEM (HRTEM) image shown in Figure 4e reveals that the shell has a distinct set of visible lattice fringes with an interplanar spacing of 0.467 nm, corresponds well to the (111) plane of spinel $NiCo_2O_4$. The core/shell structure can also be supported by EDS elemental mapping of Co, Ni and O (Figure 4f). The EDS result shows that the atomic ratio of Co: Ni is ∼1.9 in the shell, which further confirming that the spinal $NiCo_2O_4$ nanoflake shell has been prepared by CBD process combined with annealing (see the Supporting Information, Figure S1).

3.2. Electrochemical Analysis. The pseudocapacitive performance of the $NiCo_2O_4@NiCo_2O_4$ core/shell nanoflake arrays were investigated for their potential application in electrochemical energy storage. Figure 5a shows the CV curves of the bare $NiCo_2O_4$, $NiCo_2O_4@NiCo_2O_4$ core/shell nanoflake arrays and Ni foam at a scan rate of 10 mV s^{-1}. A pair of redox
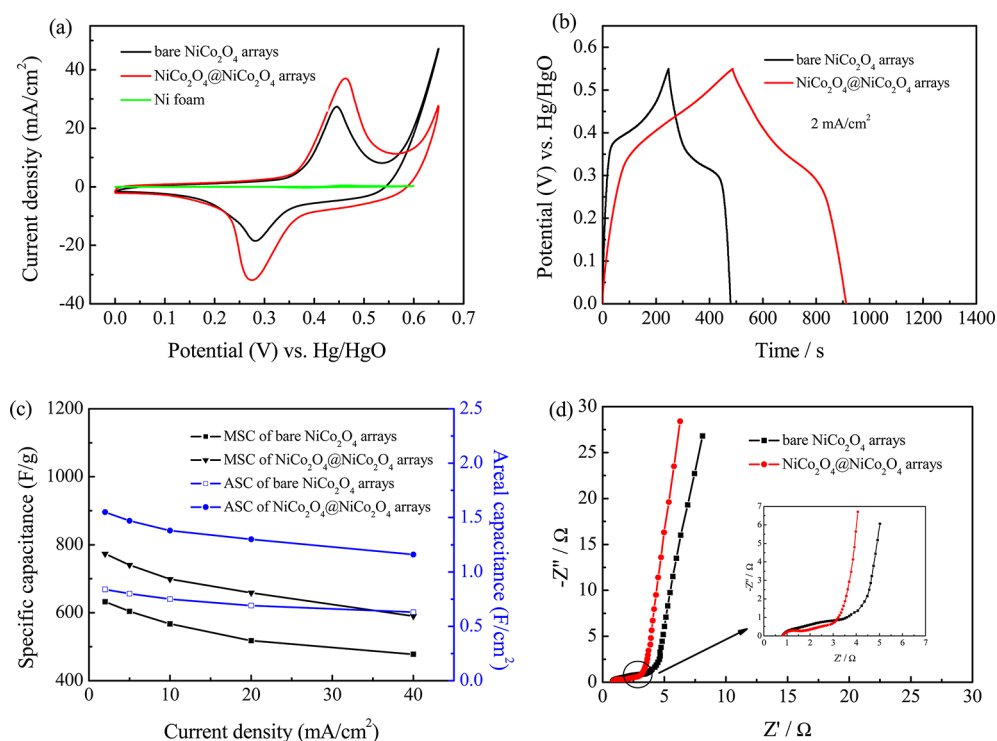
Figure 5. (a) CV curves of the bare $NiCo_2O_4$ nanoflake and $NiCo_2O_4@NiCo_2O_4$ core/shell nanoflake array electrodes at a scanning rate of 10 mV s^{-1}, (b) charge—discharge curves of the two electrodes at a current density of 2 mA cm^{-2}, (c) ASC and specific capacitance of the electrodes as a function of current density, (d) Nyquist plots of the two electrodes.

peaks at 0.28 and 0.45 V (vs Hg/HgO) are clearly observed for the bare $NiCo_2O_4$ nanoflake array, which correspond to the reversible reactions of Co^{3+}/Co^{4+} and Ni^{2+}/Ni^{3+} transitions associated with anions OH^{-}.[54,55] The redox reactions in the alkaline electrolyte are based on the following equations

$$NiCo_2O_4 + OH^- + H_2O \leftrightarrow NiOOH + 2CoOOH + e^- \tag{2}$$

$$CoOOH + OH^- \leftrightarrow CoO_2 + H_2O + e^- \tag{3}$$
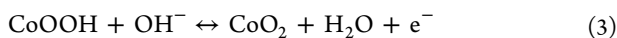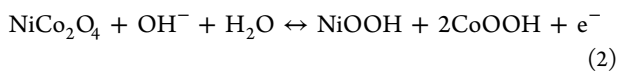
Remarkably, a similar CV shape is still found for the core–shell nanoflake arrays. Furthermore, the area integrated within the current—potential curve is much larger than that of the bare one, indicating that the core/shell nanoflake arrays have higher electrochemical reaction activity. It should be attributed to the additional pseudocapacitance contributed by the $NiCo_2O_4$ shell. To check the substrate effect of Ni foam, we also present the CV curve of nickel foam. Compared to the bare $NiCo_2O_4$ and $NiCo_2O_4@NiCo_2O_4$ core/shell nanoflake arrays, the signal of nickel foam is quite small, indicating that the nickel foam contributes little to the total capacitance of the electrode.

Galvanostatic charge—discharge tests were further performed in the voltage range of 0–0.55 V to estimate the capacitance of the two array electrodes. Figure 5b shows the discharge capacitance of the bare $NiCo_2O_4$ and $NiCo_2O_4@NiCo_2O_4$ core/shell nanoflake arrays at a current density of 2 mA cm^{-2}. Evidently, the core/shell nanoflake array electrode delivers a much higher specific capacitance than the bare one. Meanwhile, the discharge areal capacitance of the core/shell nanoflake array electrode is calculated to be 1.55 F cm^{-2}, which is about 2 times larger than the bare one (0.84 F cm^{-2}). In addition, the specific capacitances and the ASC of the two electrodes at various discharge current densities are calculated and presented in Figure 5c. The ASC of the $NiCo_2O_4@$

$NiCo_2O_4$ core/shell nanoflake arrays are calculated to be 1.55, 1.47, 1.38, 1.3, and 1.16 F cm^{-2} at the discharge current densities of 2, 5, 10, 20, and 40 mA cm^{-1} respectively, much higher than those of the bare $NiCo_2O_4$ arrays, whose capacitance is just 0.84 and 0.63 F cm^{-2} at 2 and 40 mA cm^{-2}. Besides, the specific capacitances of the core/shell nanoflake arrays are superior to those of the bare one, which can be also seen in Figure 5c. ASC of the $NiCo_2O_4@NiCo_2O_4$ core/shell nanoflake arrays reported here is superior to other previously reported core/shell nanowire array nanoarchitectures, such as Co_3O_4–NiO core/shell nanowire arrays (1.35 F cm^{-2} at 6 mA cm^{-2}),[29] Co_3O_4–MnO_2 core/shell nanowire arrays (0.56 F cm^{-2} at 11.25 mA cm^{-2}),[50] $Fe_3O_4@SnO_2$ core/shell nanorod film (7.013 mF cm^{-2} at 0.20 mA cm^{-2}).[49] Ni–NiO core/shell inverse opal film (8–9 mF cm^{-2}).[56] MnO_2–NiO core/shell nanowire arrays (0.35 F cm^{-2} at 9.5 mA cm^{-2}),[1] etc. Such high ASC at large current densities further proves the great advantages of the present core/shell nanoflake arrays.

The enhanced ion diffusion and effective electron transfer in the core/shell nanoflake arrays are further confirmed by the EIS measurements (Figure 5d). The inset shows the semicircle evident at high frequency. The impedance spectra of the $NiCo_2O_4@NiCo_2O_4$ core/shell and bare $NiCo_2O_4$ arrays are similar in form with a quasi-semicircle at a higher frequency region and a linear part at lower frequency. The linear part corresponds to the Warburg impedance (W), which is described as a diffusive impendence of the OH^{-} ion within the electrode. The slopes of the straight line at low frequency of the two electrodes are almost the same, indicating nearly the equal value of the electrolyte diffusion impendence. In addition, the semicircle of the Nyquist diagram corresponds to the Faradic reactions and its diameter represents the interfacial charge-transfer impendence. The charge-transfer impendence

of the NiCo$_2$O$_4$@NiCo$_2$O$_4$ core/shell nanoflake arrays is smaller than that of the bare one. The results above demonstrate that the combination of fast ion diffusion as well as low electron-transfer resistance is also responsible for the enhanced electrochemical performance of the core/shell nanoflake arrays.

The enhancement in the supercapacitor performance of the NiCo$_2$O$_4$@NiCo$_2$O$_4$ core/shell nanoflake array electrode can be also manifested by its excellent cycling stability. Figure 6

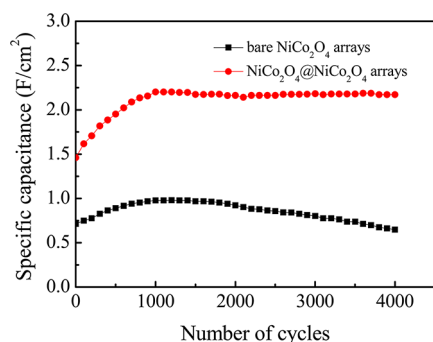**Figure 6.** Areal specific capacitance as a function of cycle number of the bare NiCo$_2$O$_4$ nanoflake and NiCo$_2$O$_4$@NiCo$_2$O$_4$ core/shell nanoflake array electrodes between 0 and 0.5 V at a current density of 5 mA cm^{-2}.

shows the cyclability of the bare NiCo$_2$O$_4$ and NiCo$_2$O$_4$@ NiCo$_2$O$_4$ core/shell array electrodes over 4000 cycles between 0 and 0.5 V at a current density of 5 mA cm^{-2}. It can be observed that the specific capacitance of both the electrodes increase gradually in the first 1000 cycles, which can be attributed to the complete activation of the electrode. The areal specific capacitance of the NiCo$_2$O$_4$@NiCo$_2$O$_4$ core/shell nanoflake array and the bare one reach a maximum value of 2.20 and 0.98 F cm^{-2} after activation, respectively. Remarkably, the cycling stability is largely enhanced in the core−shell nanoflake array electrode. It shows a specific capacitance of 2.17 F cm^{-2} after 4000 cycles and keeps 98.6% of the highest value, much higher than the bare one (0.65 F cm^{-2} with 66.3%). Similar result can also been obtained by comparing the mass specific capacitance (see information in Figure S2). The specific capacitance of the NiCo$_2$O$_4$@NiCo$_2$O$_4$ core/shell nanoflake array can achieve a maximum of 1115.6 F g^{-1} at a current density of 5 mA cm^{-2}, which can still retain 1100.2 F g^{-1} after 4000 cycles. The cycling performance of the core/shell nanoflake arrays is much better than that of the other NiCo$_2$O$_4$-based nanostructures, such as NiCo$_2$O$_4$@MnO$_2$ core/shell heterostructured nanowire arrays (12% loss after 2000 cycles),[45] hierarchical porous NiCo$_2$O$_4$ nanowires (~6.2% loss after 3000 cycles),[3] single-crystalline NiCo$_2$O$_4$ nanoneedle arrays (~5.26% loss after 2000 cycles),[2] NiCo$_2$O$_4$ nanowires (~19% loss after 3000 cycles).[32] Thus, the unique array electrode shows high electrochemical stability for long cycle life applications at high current densities.

Several contributing factors can be considered for the high specific capacitance and excellent cycling stability of the NiCo$_2$O$_4$@NiCo$_2$O$_4$ core/shell nanoflake arrays. First, the large opened "V-type" channels between nanoflakes enable the full exposure of the arrays to the electrolyte. The open geometry between the arrays allows easier electrolyte penetration into the inner region of the electrode, increasing the utilization of the active materials. Second, the NiCo$_2$O$_4$

nanoflake shells prepared by CBD method are well wrapped on the surface of NiCo$_2$O$_4$ nanoflakes prepared by hydrothermal method. It could provide facile electron transport for Faradic reaction and maintain the structural integrity of the core during charge−discharge process. Third, the NiCo$_2$O$_4$ nanoflake shells are interconnected but still do not fully cover the entire NiCo$_2$O$_4$ core. Even the core NiCo$_2$O$_4$ nanoflakes are highly accessible to electrolyte for energy storage. Therefore, nearly all the core−shell nanoflakes are highly accessible to electrolyte to obtain a high specific capacitance. Besides, as both the "core" and the "shell" are ultrathin, the electrolyte can diffuse into the underneath part of the electrode materials, so all the active materials can participate in the electrochemical charge storage process, leading to a higher area specific capacitance. Fourth, the core NiCo$_2$O$_4$ nanoflakes connect with each other, forming a flake network. The nanoflakes support each other, making the structure stable. Such a stable and connecting structure helps to alleviate the structure damage caused by volume expansion during cycling process, resulting in an enhanced stability.

4. CONCLUSIONS

In summary, homogeneous NiCo$_2$O$_4$@NiCo$_2$O$_4$ core/shell nanoflake arrays have been fabricated on Ni foam as a binder-free electrode for high-performance supercapacitors. The ultrathin NiCo$_2$O$_4$ nanoflake arrays synthesized by hydro-thermal method are the "core" while the NiCo$_2$O$_4$ nanoflakes prepared by chemical bath deposition are the "shell". The core/shell nanoflake array electrode exhibits excellent pseudocapacitive behaviors with high specific capacitance and good cycling stability. Its outstanding electrochemical performance comes from the porous core/shell configuration, which provides fast ion and electron transfer, large number of active sites and good strain accommodation.

■ ASSOCIATED CONTENT

Ⓢ Supporting Information
Figures S1 shows the EDS analysis for the shell part of the NiCo$_2$O$_4$@NiCo$_2$O$_4$ core/shell nanoflake. Figures S2 depicts the specific capacitance as a function of cycle number of the bare NiCo$_2$O$_4$ and NiCo$_2$O$_4$@NiCo$_2$O$_4$ core/shell nanoflake array electrodes between 0 and 0.5 V at a current density of 5 mV cm^{-2}. This material is available free of charge via the Internet at http://pubs.acs.org/.

■ AUTHOR INFORMATION

Corresponding Author
*E-mail: tujp@zju.edu.cn or tujplab@zju.edu.cn. Tel.: +86-571-87952856. Fax: +86-571-87952573.

Notes
The authors declare no competing financial interest.

■ ACKNOWLEDGMENTS

■ REFERENCES

(1) Liu, J. P.; Jiang, J.; Bosman, M.; Fan, H. J. *J. Mater. Chem.* **2012**, *22*, 2419−2426.
(2) Zhang, G. Q.; Wu, H. B.; Hoster, H. E.; Chan-Park, M. B.; Lou, X. W. *Energy Environ. Sci.* **2012**, *5*, 9453−9456.
(3) Jiang, H.; Ma, J.; Li, C. Z. *Chem. Commun.* **2012**, *48*, 4465−4467.
(4) Cui, B.; Lin, H.; Li, J. B.; Li, X.; Yang, J.; Tao, J. *Adv. Funct. Mater.* **2008**, *18*, 1440−1447.

(5) Zhang, G.; Lou, X. W. *Sci. Rep.* **2013**, *3*, No. 1470.

(6) Xia, X. H.; Tu, J. P.; Mai, Y. J.; Chen, R.; Wang, X. L.; Gu, C. D.; Zhao, X. B. *Chem.—Eur. J.* **2011**, *17*, 10898−10905.

(7) Karthikeyan, K.; Kalpana, D.; Renganathan, N. G. *Ionics* **2008**, *15*, 107−110.

(8) Wang, F. X.; Xiao, S. Y.; Hou, Y. Y.; Hu, C. L.; Liu, L. L.; Wu, Y. P. *RSC Adv.* **2013**, *3*, 13059−13084.

(9) Xia, X. H.; Tu, J. P.; Zhang, Y. Q.; Mai, Y. J.; Wang, X. L.; Gu, C. D.; Zhao, X. B. *RSC Adv.* **2012**, *2*, 1835−1841.

(10) Xia, X. H.; Tu, J. P.; Mai, Y. J.; Wang, X. L.; Gu, C. D.; Zhao, X. B. *J. Mater. Chem.* **2011**, *21*, 9319−9325.

(11) Zhang, Y. Q.; Xia, X. H.; Kang, J.; Tu, J. P. *Chin. Sci. Bull.* **2012**, *57*, 4215−4219.

(12) Zhang, Y. Q.; Xia, X. H.; Tu, J. P.; Mai, Y. J.; Shi, S. J.; Wang, X. L.; Gu, C. D. *J. Power Sources* **2012**, *199*, 413−417.

(13) Han, J. B.; Dou, Y. B.; Zhao, J. W.; Wei, M.; Evans, D. G.; Duan, X. *Small* **2013**, *9*, 98−106.

(14) Lu, X. H.; Zhai, T.; Zhang, X. H.; Shen, Y. Q.; Yuan, L. Y.; Hu, B.; Gong, L.; Chen, J.; Gao, Y. H.; Zhou, J.; Tong, Y. X.; Wang, Z. L. *Adv. Mater.* **2012**, *24*, 938−944.

(15) Xiao, X.; Ding, T. P.; Yuan, L. Y.; Shen, Y. Q.; Zhong, Q.; Zhang, X. H.; Cao, Y. Z.; Hu, B.; Zhai, T.; Gong, L.; Chen, J.; Tong, Y. X.; Zhou, J.; Wang, Z. L. *Adv. Energy Mater.* **2012**, *2*, 1328−1332.

(16) Zheng, H. M.; Zhai, T.; Yu, M. H.; Xie, S. L.; Liang, C. L.; Zhao, W. X.; Wang, S. C. I.; Zhang, Z. S.; Lu, X. H. *J. Mater. Chem. C* **2013**, *1*, 225−229.

(17) Xia, X. H.; Tu, J. P.; Zhang, Y. Q.; Mai, Y. J.; Wang, X. L.; Gu, C. D.; Zhao, X. B. *J. Phys. Chem. C* **2011**, *115*, 22662−22668.

(18) Xia, Q. X.; Hui, K. S.; Hui, K. N.; Hwang, D. H.; Lee, S. K.; Zhou, W.; Cho, Y. R.; Kwon, S. H.; Wang, Q. M.; Son, Y. G. *Mater. Lett.* **2012**, *69*, 69−71.

(19) Xia, X. H.; Tu, J. P.; Zhang, J.; Wang, X. L.; Zhang, W. K.; Huang, H. *Sol. Energy Mater. Sol. Cells* **2008**, *92*, 628−633.

(20) Du, N.; Xu, Y. F.; Zhang, H.; Yu, J. X.; Zhai, C. X.; Yang, D. R. *Inorg. Chem.* **2011**, *50*, 3320−3324.

(21) Zhou, L.; Zhao, D. Y.; Lou, X. W. *Adv. Mater.* **2012**, *24*, 745−748.

(22) Guan, C.; Liu, J. P.; Cheng, C. W.; Li, H. X.; Li, X. L.; Zhou, W. W.; Zhang, H.; Fan, H. J. *Energy Environ. Sci.* **2011**, *4*, 4496−4499.

(23) Huang, H.; Zhu, W. J.; Tao, X. Y.; Xia, Y.; Yu, Z. Y.; Fang, J. W.; Gan, Y. P.; Zhang, W. K. *ACS Appl. Mater. Interfaces* **2012**, *4*, 5974−5980.

(24) Xia, X. H.; Tu, J. P.; Wang, X. L.; Gu, C. D.; Zhao, X. B. *J. Mater. Chem.* **2011**, *21*, 671−679.

(25) Zhang, X. J.; Shi, W. H.; Zhu, J. X.; Zhao, W. Y.; Ma, J.; Mhaisalkar, S.; Maria, T. L.; Yang, Y. H.; Zhang, H.; Hng, H. H.; Yan, Q. Y. *Nano Res.* **2010**, *3*, 643−652.

(26) Yuan, C. Z.; Zhang, X. G.; Su, L. H.; Gao, B.; Shen, L. F. *J. Mater. Chem.* **2009**, *19*, 5772−5777.

(27) Yang, S. H.; Song, X. F.; Zhang, P.; Gao, L. *ACS Appl. Mater. Interfaces* **2013**, *5*, 3317−3322.

(28) Li, Q.; Wang, Z. L.; Li, G. R.; Guo, R.; Ding, L. X.; Tong, Y. X. *Nano Lett.* **2012**, *12*, 3803−3807.

(29) Xia, X. H.; Tu, J. P.; Zhang, Y. Q.; Wang, X. L.; Gu, C. D.; Zhao, X. B.; Fan, H. J. *ACS Nano* **2012**, *6*, 5531−5538.

(30) Xiao, J. W.; Yang, S. H. *RSC Adv.* **2011**, *1*, 588−595.

(31) Wang, X.; Han, X. D.; Lim, M.; Singh, N.; Gan, C. L.; Jan, M.; Lee, P. S. *J. Phys. Chem. C* **2012**, *116*, 12448−12454.

(32) Wang, H. L.; Gao, Q. M.; Jiang, J. *Small* **2011**, *7*, 2454−2459.

(33) Wang, C. H.; Zhang, X.; Zhang, D. C.; Yao, C.; Ma, Y. W. *Electrochim. Acta* **2012**, *63*, 220−227.

(34) Hu, L. F.; Wu, L. M.; Liao, M. Y.; Hu, X. H.; Fang, X. S. *Adv. Funct. Mater.* **2012**, *22*, 998−1004.

(35) Xiao, J. W.; Yang, S. H. *J. Mater. Chem.* **2012**, *22*, 12253−12262.

(36) Wang, H. W.; Hu, Z. A.; Chang, Y. Q.; Chen, Y. L.; Wu, H. Y.; Zhang, Z. Y.; Yang, Y. Y. *J. Mater. Chem.* **2011**, *21*, 10504−10511.

(37) Du, J.; Zhou, G.; Zhang, H. M.; Cheng, C.; Ma, J. M.; Wei, W. F.; Chen, L. B.; Wang, T. H. *ACS Appl. Mater. Interfaces* **2013**, *5*, 7405−7409.

(38) Li, Q. F.; Zeng, L. X.; Wang, J. C.; Tang, D. P.; Liu, B. Q.; Chen, G. N.; Wei, M. D. *ACS Appl. Mater. Interfaces* **2011**, *3*, 1366−1373.

(39) Liu, M. C.; Kong, L. B.; Lu, C.; Li, X. M.; Luo, Y. C.; Kang, L. *ACS Appl. Mater. Interfaces* **2012**, *4*, 4631−4636.

(40) Cabo, M.; Pellicer, E.; Rossinyol, E.; Estrader, M.; López-Ortega, A.; Nogués, J.; Castell, O.; Suriñach, S.; Baró, M. D. *J. Mater. Chem.* **2010**, *20*, 7021−7028.

(41) Jiang, H.; Li, C. Z.; Sun, T.; Ma, J. *Chem. Commun.* **2012**, *48*, 2606−2608.

(42) Wang, H. W.; Wang, X. F. *ACS Appl. Mater. Interfaces* **2013**, *5*, 6255−6260.

(43) Liu, M. C.; Kong, L. B.; Lu, C.; Ma, X. J.; Li, X. M.; Luo, Y. C.; Kang, L. *J. Mater. Chem. A* **2013**, *1*, 1380−1387.

(44) Liu, X. Y.; Zhang, Y. Q.; Xia, X. H.; Shi, S. J.; Lu, Y.; Wang, X. L.; Gu, C. D.; Tu, J. P. *J. Power Sources* **2013**, *239*, 157−163.

(45) Yu, L.; Zhang, G. Q.; Yuan, C. Z.; Lou, X. W. *Chem. Commun.* **2013**, *49*, 137−139.

(46) Jiang, H.; Ting, Z.; Li, C. Z.; Ma, J. *J. Mater. Chem.* **2011**, *21*, 3818−3823.

(47) Yuan, C. Z.; Li, J. Y.; Hou, L. R.; Yang, L.; Shen, L. F.; Zhang, X. G. *J. Mater. Chem.* **2012**, *22*, 16084−16090.

(48) Yuan, C. Z.; Li, J. Y.; Hou, L. R.; Zhang, X. G.; Shen, L. F.; Lou, X. W. *Adv. Funct. Mater.* **2012**, *22*, 4592−4597.

(49) Li, R. Z.; Ren, X.; Zhang, F.; Du, C.; Liu, J. P. *Chem. Commun.* **2012**, *48*, 5010−5012.

(50) Liu, J. P.; Jiang, J.; Cheng, C. W.; Li, H. X.; Zhang, J. X.; Gong, H.; Fan, H. J. *Adv. Mater.* **2011**, *23*, 2076−2081.

(51) Kim, J. Y.; Lee, S. H.; Yan, Y. F.; Oh, J.; Zhu, K. *RSC Adv.* **2012**, *2*, 8281−8285.

(52) Tang, W.; Gao, X. W.; Zhu, Y. S.; Yue, Y. B.; Shi, Y.; Wu, Y. P.; Zhu, K. *J. Mater. Chem.* **2012**, *22*, 20143−20145.

(53) Qu, Q. T.; Zhu, Y. S.; Gao, X. W.; Wu, Y. P. *Adv. Energy Mater.* **2012**, *2*, 950−955.

(54) Li, Y. G.; Hasin, P.; Wu, Y. Y. *Adv. Mater.* **2010**, *22*, 1926−1929.

(55) Cao, L.; Lu, M.; Li, H. L. *J. Electrochem. Soc.* **2005**, *152*, A871−A875.

(56) Kim, J. H.; Kang, S. H.; Zhu, K.; Kim, J. Y.; Neale, N. R.; Frank, A. J. *Chem. Commun.* **2011**, *47*, 5214−5216.